Atherosclerosis 288 (2019) 168–174

Contents lists available at ScienceDirect

Atherosclerosis

journal homepage: www.elsevier.com/locate/atherosclerosis

Prediction of coronary thin-cap fibroatheroma by intravascular ultrasound-based machine learning

Youngoh Bae[a,1], Soo-Jin Kang[a,*,1], Geena Kim[b], June-Goo Lee[c], Hyun-Seok Min[a], Hyungjoo Cho[a], Do-Yoon Kang[a], Pil Hyung Lee[a], Jung-Min Ahn[a], Duk-Woo Park[a], Seung-Whan Lee[a], Young-Hak Kim[a], Cheol Whan Lee[a], Seong-Wook Park[a], Seung-Jung Park[a]

[a] Department of Cardiology, University of Ulsan College of Medicine, Asan Medical Center, Seoul, South Korea
[b] College of Computer & Information Sciences, Regis University, Denver, CO, USA
[c] Biomedical Engineering Research Center, Asan Institute for Life Sciences, Seoul, South Korea

HIGHLIGHTS

- Machine learning provides the ability to automatically learn without being explicitly programmed, which enables improving diagnostic accuracies.
- The models using computed IVUS features predict the presence of OCT-derived thin-cap fibroatheromas with an overall accuracy > 80%.
- The data-driven approach may help clinicians identify high-risk coronary lesions.

ARTICLE INFO

Keywords:
Machine learning
Intravascular ultrasound
Thin-cap fibroatheroma

ABSTRACT

Background and aims: Although grayscale intravascular ultrasound (IVUS) is commonly used for assessing coronary lesion morphology and optimizing stent implantation, detection of vulnerable plaques by IVUS remains challenging. We aimed to develop machine learning (ML) models for predicting optical coherence tomography-derived thin-cap fibroatheromas (OCT-TCFAs).

Methods: In 517 patients with angina, 414 and 103 coronary lesions were randomized into training *vs.* test sets. Each of the IVUS-OCT co-registered frames (including 32,807 for training and 8101 for test) was labeled according to the presence *vs.* absence of OCT-TCFA. Among 1449 computed IVUS features based on two-dimensional geometry and texture, 17 features were finally selected and used in supervised ML with artificial neural network (ANN), support vector machine (SVM), and naïve Bayes.

Results: IVUS sections with (*vs.* without) OCT-TCFA showed a larger plaque burden, and a smaller and eccentric lumen. TCFA-containing sections were characterized by increased ratios of variance, entropy, and kurtosis; reduced ratio of homogeneity within the superficial to the deeper plaque; and decreased smoothness within the fibrous cap. In addition, OCT-TCFA was associated with low ratios of gamma-beta, Nakagami-μ and Nakagami-ω, and a high ratio of Rayleigh-b within the superficial to the deeper region. With a 5-fold cross-validation, the averaged accuracies were 81 ± 5% for ANN (area under the curve [AUC] = 0.80 ± 0.08), 77 ± 4% for SVM (AUC = 0.74 ± 0.05), and 78 ± 2% for naïve Bayes (AUC = 0.77 ± 0.04) for predicting OCT-TCFA. In the test set, ANN and naïve Bayes showed the overall accuracies of > 80%.

Conclusions: Supervised ML algorithms with computed IVUS features predicted the presence of OCT-TCFA. This data-driven approach may help clinicians in recognizing high-risk coronary lesions.

1. Introduction

For stratifying the risk of cardiovascular events, it is important to recognize a precursor of plaque rupture that leads to acute coronary thrombosis or rapid lesion progression. Thin-cap fibroatheroma (TCFA), as a morphological substrate prone to rupture, is characterized by a

* Corresponding author. Dept. of Cardiology, Asan Medical Center, University of Ulsan College of Medicine, 88, Olympic-ro 43-gil, Songpa-gu, Seoul, 05505, South Korea.
E-mail addresses: sjkang@amc.seoul.kr, sjkang3157@gmail.com (S.-J. Kang).
[1] These authors contributed equally to this work.

https://doi.org/10.1016/j.atherosclerosis.2019.04.228
Received 6 December 2018; Received in revised form 16 April 2019; Accepted 30 April 2019
Available online 04 May 2019
0021-9150/

large necrotic core, a thin-fibrous cap, and infiltration of rare smooth muscle cells but numerous macrophages [1,2]. Previous studies evaluating the natural history of non-culprit lesions suggested that the presence of TCFA was an independent predictor of adverse cardiac outcomes [3–5].

For in vivo detection of TCFA-containing lesions, optical coherence tomography (OCT) is considered a gold standard, whereas grayscale intravascular ultrasound (IVUS) has been practically utilized in assessing lesion morphology, device sizing, and stent optimization. Moreover, the clinical impact of IVUS-guided percutaneous coronary intervention (PCI) has been validated with abundant data [6–9]. Nonetheless, the identification of vulnerable plaques with IVUS remains challenging owing to the poor spatial resolution of 150–200 μm relative to the histological threshold of the thin cap (< 65 μm) and the shortcoming of IVUS in tissue characterization.

Machine learning (ML) techniques have emerged as highly effective computer algorithms for recognizing patterns in large datasets with a multitude of variables, and for building models for data-driven prediction [10–12]. The aims of this study using 41,101 IVUS-OCT co-registered sections in 517 coronary arteries were (i) to identify the geometry- and texture-based computed IVUS features for predicting the presence of an OCT-derived TCFA (OCT-TCFA), and (ii) to develop supervised ML models for classifying sections with *vs.* without OCT-TCFA.

2. Materials and methods

2.1. Study population

Between May 2010 and January 2015, consecutive 5378 patients with stable and unstable angina underwent invasive coronary angiography at Asan Medical Center, Seoul, Korea. Both pre-procedural IVUS and OCT data for assessing lesions with an angiographic diameter stenosis of 30–80% on visual estimation were obtained in 692 patients. When multiple lesions were evaluated in a patient, the lesion with the highest degree of angiographic stenosis was selected. Excluding 155 stented lesions and 20 lesions with poor imaging quality, a total of 517 coronary lesions in 517 patients were enrolled in this study (Table 1). To avoid adjacent frames with similar characteristics being enrolled into both the training and test sets, per-patient randomization was done. With a ratio of 4:1, 414 and 103 patients were randomly separated into the training and testing samples, respectively. All patients provided written informed consent, and the institutional review board of Asan Medical Center approved the study.

Table 1
Baseline characteristics in 517 patients with 517 coronary lesions.

Clinical data	
Age, years	65.0 ± 9.9
Men	382 (74%)
Diabetes mellitus	145 (28%)
Hypertension	315 (61%)
Current smoker	233 (45%)
Hyperlipidemia	284 (55%)
Acute coronary syndrome	150 (29%)
Quantitative angiographic data	
Involved vessel	
Left anterior descending artery lesion	284 (55%)
Left circumflex artery lesion	119 (23%)
Right coronary artery lesion	165 (32%)
Diameter stenosis, %	50.9 ± 11.8
Minimal lumen diameter, mm	1.6 ± 0.5
Lesion length, mm	17.1 ± 10.2
Proximal RLD, mm	3.3 ± 0.6
Distal RLD, mm	2.9 ± 0.6

RLD, reference lumen diameter.

2.2. Angiographic measurements

To provide the lesion characteristics, quantitative coronary angiography was performed using standard techniques with automated edge-detection algorithms (CAAS-5; Pie-Medical, Netherlands). Angiographic diameter stenosis, minimal lumen diameter, lesion length, and the proximal and distal reference lumen diameters were measured.

2.3. Acquisition of IVUS and OCT

After intracoronary administration of 0.2 mg nitroglycerin, grayscale IVUS imaging was done using motorized transducer pullback (0.5 mm/s) and a commercial scanner (Boston Scientific/SCIMED, Minneapolis, MN), consisting of a rotating, 40-MHz transducer within a 3.2-F imaging sheath. OCT images were acquired using a non-occlusive technique with the C7XR™ system and DragonFly™ catheters (LightLab Imaging, Inc.) at a pullback speed of 20 mm/s.

Attenuated plaque, a conventional IVUS parameter of lipid-rich plaque, was defined as ultrasonic attenuation despite the absence of calcium. The angle of attenuation was measured with an electronic protractor centered on the lumen.

2.4. Co-registration of IVUS and OCT

A lesion included sections with > 0.5 mm maximal plaque thickness. Every OCT frame with a 0.4-mm interval was co-registered with its comparable IVUS frame (approximately every 24th IVUS frame) by using anatomical landmarks such as vessel shape, side branches, calcium, perivascular structures, and distance from the ostium. Excluding the sections at the branching site, 41,101 IVUS-OCT matched frames in 517 lesions were obtained. Each IVUS frame was labeled according to the presence *vs.* absence of OCT-derived TCFA (OCT-TCFA). In this study, OCT-TCFA was defined as an OCT-delineated necrotic core with an angle ≥90° and an overlying fibrous cap thickness of < 200 μm (corresponding to the resolution limit of grayscale IVUS) at the thinnest part. OCT images were analyzed by two independent investigators in the imaging core laboratory at Asan Medical Center. When there was discordance between the observers, a consensus reading was obtained.

2.5. IVUS segmentation

Lumen segmentation was done using the interface between the lumen and the leading edge of the intima (Supplemental Fig. 1). A discrete interface at the border between the media and the adventitia corresponded almost to the location of the external elastic membrane (EEM). As pre-processing, automatic segmentation of IVUS images was performed using the FCN-at-one-VGG16 algorithm (Supplemental Methods). All segmented frames were meticulously reviewed by experts, and wrong segmentations were manually corrected in 22% of the overall IVUS sections.

2.6. Region-of-interest extraction

IVUS frames were segmented into three compartments, as follows: (i) adventitia including the pixels outside the EEM (coded as “0”), (ii) lumen including the pixels within the lumen border (coded as “1”), and (iii) plaque including the pixels between the lumen border and EEM (coded as “2”), which was the region of interest. On the masked image, the intra-plaque area was further segmented into five regions (S_1–S_5): S_1 defined as the 2-pixel (32.2 μm)-thickness region adjacent to the lumen border, S_2 defined as the 4-pixel (64.4 μm)-thickness region from the edge of S_1, S_3 defined as the 7-pixel (109.2 μm)-thickness region from the edge of S_2, S_4 defined as the 13-pixel (202.8 μm)-thickness region from the edge of S_3, and S_5 defined as the remaining region adjacent to the EEM (Supplemental Fig. 1).

2.7. Computational feature extraction

The computed IVUS features were generated after filtering (with a 4 × 4 median filter) of scattered and noised images. They consisted of three categories, as follows: (i) two-dimensional geometry-based features including plaque burden, minimal lumen diameter, lumen area, and lumen eccentricity; (ii) probability distribution parameters including gamma-beta, Nakagami-μ, Nakagami-ω, and Rayleigh-b; and (iii) texture-based features including variance, moment, smoothness, kurtosis, entropy, and homogeneity (Supplemental Table 1 and Supplemental Methods). They were obtained within the entire plaque and each of the five segments (S_1–S_5). With the inclusion of the ratios of the computed features between two different segments (S_1:S_2, S_1:S_3, S_1:S_4, S_1:S_5, S_2:S_3, S_2:S_4, S_2:S_5, S_3:S_4, S_3:S_5, and S_4:S_5), 1449 features were extracted. Feature extraction and selection was performed on the training set.

2.8. Feature selection

To distinguish the sections with *vs.* without OCT-TCFA, a total of 17 features were selected by using multi-stage feature selection methods, as follows: First, 728 features of 1449 computed features were selected using *t*-test ($p < 0.05$). Among the 728 features, 62 features with an area under the curve (AUC) of > 0.6 were selected by using receiver operating curve (ROC) analysis for predicting OCT-TCFA, and then used in various feature selection methods such as relief, decision tree, regularized discriminative feature selection for unsupervised learning, sort features, and Fisher's exact test (all alpha = 0.05, Supplemental Methods). By identifying the top 10 features on each selecting algorithm (Relief, Decision tree, RDFS, SF, and Fisher's exact test), the non-overlapping 17 features including plaque burden, lumen area, minimal lumen diameter, lumen eccentricity, gamma–beta S_3/S_4, Nakagami–μ S_3/S_4, Nakagami–ω S_1/S_3, Rayleigh–b S_2/S_3, variance S_2/S_3, variance S_2/S_4, entropy S_2/S_3, kurtosis S_2/S_4, homogeneity1 S_3/S_4, homogeneity2 S_2/S_4, smoothness S_1/S_3, smoothness S_2/S_3, and moment S_1/S_3 were finally selected and used in ML. The quality and relevancy of each feature was checked by stability test (Supplemental Table 2). In addition, 34 features were chosen by recursive forward selection method, and used for developing an artificial neural network model.

2.9. Machine learning

After excluding 198 IVUS frames with outlier features having values outside the 1st–99th percentile, a total of 40,908 frames (32,807 in the training set and 8101 in the test set) were used for supervised ML. The theoretical overviews and technical details of each algorithm are described in the Supplemental Methods. Using the 17 selected features from the training data, the ML models such as support vector machine (SVM) using the radial basis function kernel (C = 100 as default, gamma = 1/17, by using LibSVM), Naïve Bayes using Gaussian kernel (1-by-2 numeric row vector for eliminating skewed data), and artificial neural network (ANN) were trained. Additionally, the ANN model using the overall 1449 features was developed. Supplemental Fig. 2 also shows the top 34 features that were chosen by forward selection and utilized in ANN. The ANN models had two hidden layers that contained 16 and 8 nodes in the first and second layer, respectively. For training, a scaled conjugate gradient was used for the optimization method and binary cross entropy was used for the loss function. The ROC which was based on relative performances considering the whole range of possible probability thresholds (from 0 to 1), had an area that ranged from 0.5 for classifiers without any prediction capability to 1 for perfectly classifying algorithms. The 5-fold cross-validation was used in training to avoid overfitting (Supplemental Fig. 3). Then, the performances of the developed models were evaluated in the test set.

To reduce bias, the models were independently trained and tested on the 20 different train-test random splits with a 4:1 ratio. The averaged performances of the 20 runs with the standard deviations were calculated.

To exclude the potential effect of multiple frames per vessel, the average of the overall accuracies calculated in each patient was shown. In addition, the accuracy in randomly selected 103 frames (including one frame per patient) was provided.

3. Results

3.1. Clinical and lesion characteristics

The clinical characteristics and quantitative coronary angiographic data are summarized in Table 1. The overall frequency of OCT-TCFA was 16%. In the training sample (including 414 lesions with 32,807 frames), an OCT-TCFA was seen in 5353 (16%) frames. In the test sample (including 103 lesions with 8101 frames), 1213 (15%) frames showed an OCT-TCFA. Although the arc of IVUS-attenuation > 30° was the threshold for predicting the presence of OCT-TCFA, its sensitivity and specificity in the test samples were 16% and 93%, respectively.

3.2. IVUS features predicting OCT-TCFA

Supplemental Table 3 compares the computed IVUS features between sections with *vs.* without an OCT-TCFA. The features determining the presence of OCT-TCFA were ranked by using 5 feature selection methods (Supplemental Table 4). Table 4 shows the AUCs for predicting the presence of OCT-TCFA in the 17 features including plaque burden, lumen area, minimal lumen diameter, lumen eccentricity, gamma–beta S_3/S_4, Nakagami–ω S_1/S_3, Nakagami–μ S_3/S_4, Rayleigh–b S_2/S_3, variance S_2/S_3, variance S_2/S_4, entropy S_2/S_3, kurtosis S_2/S_4, homogeneity1 S_3/S_4, homogeneity2 S_2/S_4, smoothness S_1/S_3, smoothness S_2/S_3, and moment S_1/S_3.

With regard to the two-dimensional geometry-based features, sections with (*vs.* without) OCT-TCFA showed a larger plaque burden, a smaller lumen, and a more eccentric lumen shape (Table 2). On the basis of the texture, sections containing an OCT-TCFA were characterized by increased ratios of variance, entropy, and kurtosis, and a reduced ratio of homogeneity within the superficial to the deeper intraplaque region. The OCT-TCFA was also associated with a decrease in

Table 2
Top 17 features predicting OCT-derived TCFA.

Feature	T-test[a]		Area under curve	
	With TCFA	Without TCFA	SVM	Naïve Bayes
2D-geometry-based features				
Plaque burden	0.62	0.55	0.71	0.69
Minimal diameter	2.16	2.41	0.62	0.63
Lumen area	20,460	22,255	0.60	0.61
Lumen eccentricity	0.61	0.50	0.69	0.68
Probability distribution-parameters				
Gamma–beta S_3/S_4	2.04	7.25	0.69	0.69
Nakagami–μ S_3/S_4	5.27	6.79	0.68	0.68
Nakagami–ω S_1/S_3	5.27	6.79	0.66	0.67
Rayleigh–b S_2/S_3	4.50	3.70	0.66	0.69
Texture-based features				
Variance S_2/S_3	4.93	4.20	0.71	0.69
Variance S_2/S_4	4.53	4.04	0.69	0.68
Second moment S_1/S_3	4.08	4.60	0.64	0.65
Smoothness S_1/S_3	2.91	5.40	0.66	0.64
Smoothness S_2/S_3	3.17	4.94	0.68	0.66
Kurtosis S_2/S_4	9.68	5.98	0.69	0.69
Entropy S_2/S_3	5.29	3.66	0.69	0.67
Homogeneity1 S_3/S_4	3.94	7.28	0.68	0.69
Homogeneity2 S_2/S_4	4.39	5.01	0.68	0.67

OCT, optical coherence tomography; SVM, support vector machine; TCFA, thin-cap fibroatheroma.
[a] All $p < 0.001$ (with *vs.* without TCFA) in the *t*-test.

Table 3
IVUS prediction of OCT-TCFA.

	AUC[d]	Ssensitivity	Specificity	PPV	NPV	Overall accuracy
Training samples (5-fold CV) [a]						
Support vector machine	0.74 ± 0.05	82 ± 3%	61 ± 2%	37 ± 8%	92 ± 4%	77 ± 4%
Gaussian Naïve Bayes	0.77 ± 0.04	81 ± 3%	71 ± 3%	39 ± 2%	91 ± 3%	78 ± 2%
Artificial neural network 17[e]	0.80 ± 0.08	85 ± 4%	79 ± 6%	48 ± 4%	95 ± 3%	81 ± 5%
Artificial neural network 34[f]	0.81 ± 0.05	83 ± 3%	79 ± 6%	48 ± 4%	95 ± 3%	81 ± 3%
Artificial neural network 1449[g]	0.80 ± 0.06	85 ± 3%	79 ± 5%	48 ± 4%	95 ± 3%	81 ± 2%
Test samples[b]						
Support vector machine	0.77	80%	71%	40%	93%	78%
Gaussian Naïve Bayes	0.78	80%	71%	39%	91%	80%
Artificial neural network 17[e]	0.82	82%	79%	42%	96%	82%
Artificial neural network 34[f]	0.82	82%	79%	42%	96%	82%
Artificial neural network 1449[g]	0.82	81%	79%	42%	95%	82%
Averages in test samples from 20 runs[c]						
Support vector machine	0.74 ± 0.03	84 ± 2%	61 ± 4%	33 ± 8%	90 ± 2%	76 ± 3%
Gaussian Naïve Bayes	0.77 ± 0.04	81 ± 3%	71 ± 6%	38 ± 8%	92 ± 5%	77 ± 2%
Artificial neural network 17[e]	0.80 ± 0.07	83 ± 2%	78 ± 8%	52 ± 4%	88 ± 3%	80 ± 6%
Artificial neural network 34[f]	0.80 ± 0.06	83 ± 2%	78 ± 7%	52 ± 4%	88 ± 3%	81 ± 3%
Artificial neural network 1449[g]	0.80 ± 0.06	83 ± 3%	78 ± 7%	52 ± 5%	88 ± 3%	80 ± 5%

AUC = area under the curve, CV = cross-validation, IVUS = intravascular ultrasound, NPV = negative predictive value, OCT-TCFA = optical coherence tomography-derived thin-cap fibroatheroma, PPV = positive predictive value.

[a] Average of 5-fold cross-validation in the training sample (including 32,807 frames in 414 lesions) as [mean ± 1 standard deviation].

[b] Use of features as attribute performances in the test sample (including 8101 frames in 103 lesions).

[c] Averages in the 20 test samples from the independent 20 runs of machine learning as [mean ± 1 standard deviation].

[d] Difference in AUCs (test set): $p < 0.05$ between support vector machine *vs.* artificial neural networks, $p < 0.05$ between Gaussian Naïve Bayes *vs.* artificial neural network, and $p > 0.05$ between artificial neural network 17 *vs.* 1449.

[e] Using 17 features chosen by T-test, ROC analysis and various feature selection algorithms.

[f] Using 34 features chosen by forward selection method.

[g] Using all 1449 clinical and IVUS features.

smoothness within the fibrous cap relative to the deeper region. On the basis of the probability distribution, sections with (*vs.* without) OCT-TCFA were more likely to have reduced ratios of gamma-beta, Nakagami-μ and Nakagami-ω, and increased ratio of Rayleigh-b within the superficial to the deeper intra-plaque region.

3.3. Machine learning to predict OCT-TCFA

By using the 17 computed IVUS features, the performance of each ML classifier for the prediction of the presence *vs.* the absence of an OCT-TCFA is shown in Table 3. With a 5-fold cross-validation, ANN using 17 features showed an averaged accuracy of 81 ± 5%, a sensitivity of 85 ± 4%, and a specificity of 79 ± 6% for predicting an OCT-TCFA (average AUC = 0.80 ± 0.08). Additionally, the averaged accuracies of SVM, and Naïve Bayes were 77 ± 4% and 78 ± 2%, respectively. The averaged accuracies of 20 independent repetitions were 80 ± 6% for ANN using 17 features (AUC = 0.80 ± 0.07), 77 ± 2% for naïve Bayes (AUC = 0.77 ± 0.04), and 76 ± 3% for SVM (AUC = 0.74 ± 0.03), (Table 3).

When the overall 1449 features were used, ANN model showed the averaged accuracies of 81 ± 2% (AUC = 0.80 ± 0.06) in the training and 82% in the test samples (AUC = 0.82).

To exclude the potential effect of multiple frames per vessel, the average of the overall accuracies per patient for predicting an OCT-TCFA was 79% for SVM, 79% for Naïve Bayes, 81% for ANN using 17 features, and 82% for ANN using 1449 features (Supplemental Table 5). In addition, the overall accuracies in 103 frames obtained by random selection of one frame per patient were shown in Supplemental Table 5. The overall flow of the development of the supervised ML model is shown in Fig. 1.

4. Discussion

TCFA, a prototype of vulnerable plaque, has been considered to be associated with plaque rupture and coronary thrombosis [1,2]. The morphological predictors for the occurrence of future events have been reported. The PROSPECT (Providing Regional Observations to Study Predictors of Events in the Coronary Tree) study suggested a plaque burden ≥70%, a minimal lumen area ≤4.0 mm^2, and/or the presence of a virtual histology-derived TCFA as predictors of non-culprit-related adverse cardiac events [3], which were also supported by the ATHEROREMO-IVUS and VIVA (virtual histology-IVUS in Vulnerable Atherosclerosis) studies [4,5]. During PCI, the presence of a TCFA increases the risk of distal embolization and peri-procedural myocardial infarction [13,14]. Previous studies suggested that high-intensity statin therapy was effective in the regression of coronary atheroma [15,16]. A baseline percent necrotic core was the independent predictor for a greater response to 1-year statin therapy in plaque stabilization [17]. In addition, high-intensity statin was associated with a significant increase in minimum fibrous cap thickness and frequent regression of TCFA [18]. Thus, to characterize coronary atheroma is important to predict clinical outcomes, and to make a decision for optimal medical treatment.

Although the prognostic implication of TCFA in deferred or treated lesions has been validated, it is unclear how to choose the appropriate imaging modality and how to integrate the information for detecting a TCFA. Even though the clinical impact of IVUS in assessing lesion severity and optimizing PCI has been established [7–9], the detection of vulnerable plaques with IVUS remains challenging. The spatial resolution of 40–45 MHz grayscale IVUS (150–200 μm) is insufficient to identify the thin cap and to assess tissue composition. With an excellent resolution of 15–20 μm, a near-infrared light-based OCT is the gold standard for in vivo detection of TCFA. Although OCT is useful for evaluating the microstructures and the fibrous cap thickness, its poor penetration depth and the attenuation of light transmitted through the atheroma limit the clinical utility of OCT in estimating the plaque burden and vessel size as the important factors during PCI [19–22]. Thus, the precise assessment of both geometry and composition requires the complementary use of IVUS and OCT, which is expensive.

A few IVUS findings have been suggestive of the presence of TCFA. IVUS attenuation and spotty calcium corresponded to histologic fibroatheroma with a large necrotic core in human coronary arteries

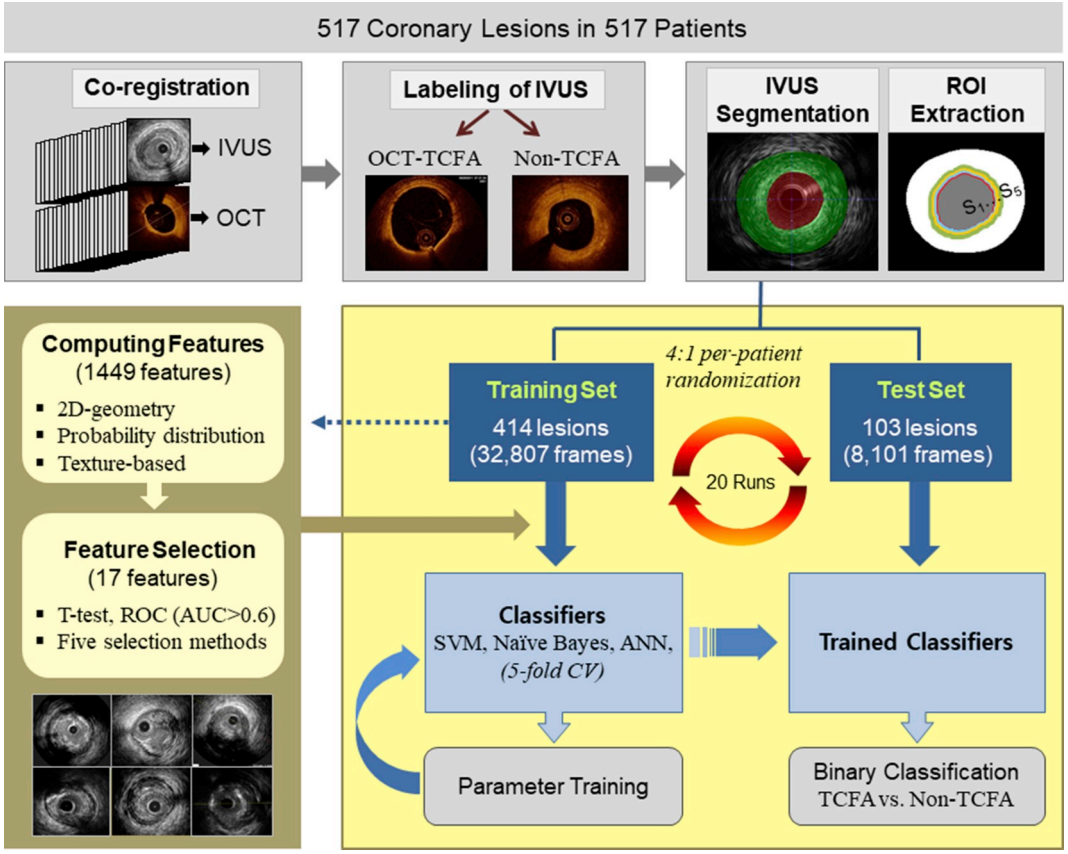

Fig. 1. Flow chart of machine learning.
2D, two-dimensional; ANN, artificial neural network; AUC , area under the curve; CV, cross-validation; IVUS, intravascular ultrasound; OCT, optical coherence tomography; ROC, receiver operating curve; ROI, region of interest; SVM, support vector machine; TCFA, thin-cap fibroatheroma.

[23]. Although the arc of IVUS attenuation of > 29.4° was the predictor of the presence of an OCT-TCFA [24], its sensitivity was only 16% in this current study. The probability of overfitting within a given dataset limited its general application. Traditional statistical methods verify the association between a specific feature and an end point, whereas they may be inadequate for developing a prediction model, especially in the setting of the complexity of features, non-linear relationship, and interactions among numerous predictive variables [10]. ML, an application of artificial intelligence, provides the ability to automatically learn without being explicitly programmed [10–12]. It attempts to balance "bias and variance," which are summarized using loss functions to preferably optimize a prediction model. In this current study, the overall accuracies of the supervised ML models were 82% by ANN, 78% by SVM, and 80% by naïve Bayes to separate IVUS sections with *vs.* without an OCT-TCFA. Ultimately, it may enhance more extensive use of IVUS in the real practice by providing both geometrical and compositional information.

This study highlighted the usefulness of geometrical factors in evaluating plaque vulnerability. It was not surprising that two-dimensional geometry-based features, including a large plaque burden and an eccentric lumen, were the predictors of OCT-TCFA. A plaque burden of ≥69% was previously shown to be the predictor of a histologic TCFA [25]. Moreover, a low endothelial shear stress had an effect on eccentric plaque development and fibrous cap thinning [26]. The cellular mechanism of accelerated atherosclerosis is mediated by the overexpression of flow-sensitive genes and alterations in vascular endothelial biology [27,28].

Furthermore, the current study provided new insights into computing IVUS features for the prediction of high-risk plaques. OCT-TCFA was characterized by increased ratios of S_2 to $S_{3\text{-}4}$ in entropy and variance, and reduced ratios of $S_{2\text{-}3}$ to S_4 in homogeneity, which suggested a greater heterogeneity in the gray level distribution at the superficial *vs.* deeper plaque. The increased ratio of S_2 to S_4 in kurtosis (a sharper peak of intensity) at the site of OCT-TCFA possibly indicated the superficial deposition of tiny calcium or cholesterol cleft. The reduced ratio of S_1 to S_3 in smoothness may suggest the infiltration of foamy macrophages or microcalcifications within the thin cap that increased the roughness. The possible but speculative explanations need to be further validated in future studies. With regard to the probability distribution parameters, gamma distribution analyzed the envelope of backscattered signals to model the local statistical properties [29,30]. Rayleigh and Nakagami distributions were applied to model small-scale fading for dense signal scatters from tissue. OCT-TCFA was associated with low ratios of gamma-beta and Nakagami-μ and Nakagami-ω within the superficial to the deeper region, and high ratios of Rayleigh-b. Although the rank in each algorithm is specific to the fitted model, the approach would be hypothesis generating and would suggest which features are valuable for being included in future studies.

4.1. Limitations

With a relatively small-sized sample, the current study using every IVUS frame with a 0.4-mm interval might have potential selection bias. With a low incidence of OCT-TCFA (16% overall), the class imbalance may have affected the results. In the multiple steps of feature selection, we excluded worthless features by using an AUC < 0.60 that might be an arbitrary threshold. With a lack of external validation, the possibility of overfitting in the given dataset cannot be excluded. The performance and clinical impact of the classifiers should be further validated in a prospective, large cohort. In addition, the used threshold of thin-cap

(< 200 μm) corresponding to the spatial resolution limit of 40-MHz IVUS was thicker than the histological criterion. Considering that many studies proved the clinical impact of TCFA defined by virtual histology-IVUS with a spatial resolution of 200–250 μm [3–5], our current ML model using the threshold of thin-cap < 200 μm would be clinically relevant. In the setting of per-frame analysis, there might be a potential clustering effect of multiple frames per vessel. However, even in the subgroup including only single frame per patient, good performances of the ML models for predicting OCT-TCFA were consistently demonstrated. Although the ML-based approach was used to better understand the unrecognized IVUS features of TCFA-containing sections, an image-based deep learning method using big data merits being attempted to achieve optimal performance for practical use.

4.2. Conclusion

Supervised ML algorithms with computed two-dimensional geometry- and texture-based features predicted TCFA-containing lesions. This data-driven approach may help clinicians in recognizing and treating high-risk coronary lesions.

Conflicts of interest

The authors declared that they do not have anything to disclose regarding conflict of interest with respect to this manuscript.

Financial support

This study was supported by grants from the Korea Healthcare Technology R&D Project, Ministry for Health & Welfare Affairs, Republic of Korea (HI15C1790 and HI17C1080); the Ministry of Science and ICT (NRF-2017R1A2B4005886); and the Asan Institute for Life Sciences, Asan Medical Center, Seoul, Korea (2017–0745).

Author contributions

SJ Kang: Conception and design of study, data interpretation, and writing the manuscript with revision.

Y Bae and JG Lee: data analysis and development of models, review and edit of the manuscript with revision.

G Kim, HS Min, H Cho: review and edit of the manuscript with revision.

DY Kang, P Lee, JM Ahn, DW Park, SW Lee, YH Kim, CW Lee, SW Park, and SJ Park: data acquisition, review and edit of the manuscript.

Appendix A. Supplementary data

Supplementary data to this article can be found online at https://doi.org/10.1016/j.atherosclerosis.2019.04.228.

References

[1] R. Virmani, A.P. Burke, A. Farb, F.D. Kolodgie, Pathology of the vulnerable plaque, J. Am. Coll. Cardiol. 47 (2006) C13–C18.
[2] A.V. Finn, M. Nakano, J. Narula, F.D. Kolodgie, R. Virmani, Concept of vulnerable/unstable plaque, Arterioscler. Thromb. Vasc. Biol. 30 (2010) 1282–1292.
[3] G.W. Stone, A. Maehara, A.J. Lansky, B. de Bruyne, E. Cristea, G.S. Mintz, R. Mehran, J. McPherson, N. Farhat, S.P. Marso, H. Parise, B. Templin, R. White, Z. Zhang, P.W. Serruys, PROSPECT Investigators. A prospective natural-history study of coronary atherosclerosis, N. Engl. J. Med. 364 (2011) 226–235.
[4] J.M. Cheng, H.M. Garcia-Garcia, S.P. de Boer, I. Kardys, J.H. Heo, K.M. Akkerhuis, R.M. Oemrawsingh, R.T. van Domburg, J. Ligthart, K.T. Witberg, E. Regar, P.W. Serruys, R.J. van Geuns, E. Boersma, In vivo detection of high-risk coronary plaques by radiofrequency intravascular ultrasound and cardiovascular outcome: results of the ATHEROREMO-IVUS study, Eur. Heart J. 35 (2014) 639–647.
[5] P.A. Calvert, D.R. Obaid, M. O'Sullivan, L.M. Shapiro, D. McNab, C.G. Densem, P.M. Schofield, D. Braganza, S.C. Clarke, K.K. Ray, N.E. West, M.R. Bennett, Association between IVUS findings and adverse outcomes in patients with coronary artery disease: the VIVA (VHIVUS in Vulnerable Atherosclerosis) Study, JACC Cardiovasc Imaging 4 (2011) 894–901.
[6] B. Witzenbichler, A. Maehara, G. Weisz, F.J. Neumann, M.J. Rinaldi, D.C. Metzger, T.D. Henry, D.A. Cox, P.L. Duffy, B.R. Brodie, T.D. Stuckey, E.L. Mazzaferri Jr., K. Xu, H. Parise, R. Mehran, G.S. Mintz, G.W. Stone, Relationship between intravascular ultrasound guidance and clinical outcomes after drug-eluting stents: the assessment of dual antiplatelet therapy with drug-eluting stents (ADAPT-DES) study, Circulation 129 (2014) 463–470.
[7] S.J. Hong, B.K. Kim, D.H. Shin, C.M. Nam, J.S. Kim, Y.G. Ko, D. Choi, T.S. Kang, W.C. Kang, A.Y. Her, Y.H. Kim, S.H. Hur, B.K. Hong, H. Kwon, Y. Jang, M.K. Hong, IVUS-XPL investigators. Effect of intravascular ultrasound-guided vs angiography-guided everolimus-eluting stent implantation: the IVUS-XPL randomized clinical trial, J. Am. Med. Assoc. 314 (2015) 2155–2163.
[8] Y.J. Zhang, S. Pang, X.Y. Chen, C.V. Bourantas, D.R. Pan, S.J. Dong, W. Wu, X.M. Ren, H. Zhu, S.Y. Shi, J. Iqbal, B.D. Gogas, B. Xu, S.L. Chen, Comparison of intravascular ultrasound guided versus angiography guided drug eluting stent implantation: a systematic review and meta-analysis, BMC Cardiovasc. Disord. 15 (2015) 153.
[9] I.Y. Elgendy, A.N. Mahmoud, A.Y. Elgendy, A.A. Bavry, Outcomes with intravascular ultrasound-guided stent implantation: a meta-analysis of randomized trials in the era of drug-eluting stents, Circ Cardiovasc Interv 9 (2016) e003700.
[10] B.A. Goldstein, A.M. Navar, R.E. Carter, Moving beyond regression techniques in cardiovascular risk prediction: applying machine learning to address analytic challenges, Eur. Heart J. 38 (2017) 1805–1814.
[11] C. Krittanawong, H. Zhang, Z. Wang, M. Aydar, T. Kitai, Artificial intelligence in precision cardiovascular medicine, J. Am. Coll. Cardiol. 69 (2017) 2657–2664.
[12] M. Henglin, G. Stein, P.V. Hushcha, J. Snoek, A.B. Wiltschko, S. Cheng, Machine learning approaches in cardiovascular imaging, Circ. Cardiovasc. Imag. 10 (2017) e005614.
[13] T. Yonetsu, T. Kakuta, T. Lee, K. Takahashi, G. Yamamoto, Y. Iesaka, et al., Impact of plaque morphology on creatine kinase-MB elevation in patients with elective stent implantation, Int. J. Cardiol. 146 (2011) 80–85.
[14] T. Lee, T. Yonetsu, K. Koura, K. Hishikari, T. Murai, T. Iwai, T. Takagi, Y. Iesaka, H. Fujiwara, M. Isobe, T. Kakuta, Impact of coronary plaque morphology assessed by optical coherence tomography on cardiac troponin elevation in patients with elective stent implantation, Circ Cardiovasc Interv 4 (2011) 378–386.
[15] S.E. Nissen, S.J. Nicholls, I. Sipahi, P. Libby, J.S. Raichlen, C.M. Ballantyne, J. Davignon, R. Erbel, J.C. Fruchart, J.C. Tardif, P. Schoenhagen, T. Crowe, V. Cain, K. Wolski, M. Goormastic, E.M. Tuzcu, ASTEROID Investigators. Effect of very high-intensity statin therapy on regression of coronary atherosclerosis: the ASTEROID trial, J. Am. Med. Assoc. 295 (2006) 1556–1565.
[16] L. Räber, M. Taniwaki, S. Zaugg, H. Kelbæk, M. Roffi, L. Holmvang, S. Noble, G. Pedrazzini, A. Moschovitis, T.F. Lüscher, C.M. Matter, P.W. Serruys, P. Jüni, H.M. Garcia-Garcia, S. Windecker, IBIS 4 (Integrated Biomarkers and Imaging Study-4) Trial Investigators. Effect of high-intensity statin therapy on atherosclerosis in non-infarct-related coronary arteries (IBIS-4): a serial intravascular ultrasonography study, Eur. Heart J. 36 (2015) 490–500.
[17] S.J. Park, S.J. Kang, J.M. Ahn, M. Chang, S.C. Yun, J.H. Roh, P.H. Lee, H.W. Park, S.H. Yoon, D.W. Park, S.W. Lee, Y.H. Kim, C.W. Lee, G.S. Mintz, K.H. Han, S.W. Park, Effect of statin treatment on modifying plaque composition: a double-blind, randomized study, J. Am. Coll. Cardiol. 67 (2016) 1772–1783.
[18] L. Räber, K.C. Koskinas, K. Yamaji, M. Taniwaki, M. Roffi, L. Holmvang, H.M. Garcia Garcia, T. Zanchin, R. Maldonado, A. Moschovitis, G. Pedrazzini, S. Zaugg, J. Dijkstra, C.M. Matter, P.W. Serruys, T.F. Lüscher, H. Kelbaek, A. Karagiannis, M.D. Radu, S. Windecker, Changes in coronary plaque composition in patients with acute myocardial infarction treated with high-intensity statin therapy (IBIS-4): a serial optical coherence tomography study, JACC Cardiovasc Imaging S1936–878X (18) (2018) 30752–30756.
[19] K. Fujii, S.G. Carlier, G.S. Mintz, Y.M. Yang, I. Moussa, G. Weisz, G. Dangas, R. Mehran, A.J. Lansky, E.M. Kreps, M. Collins, G.W. Stone, J.W. Moses, M.B. Leon, Stent underexpansion and residual reference segment stenosis are related to stent thrombosis after sirolimus-eluting stent implantation: an intravascular ultrasound study, J. Am. Coll. Cardiol. 45 (2005) 995–998.
[20] T. Okabe, G.S. Mintz, A.N. Buch, P. Roy, Y.J. Hong, K.A. Smith, R. Torguson, N. Gevorkian, Z. Xue, L.F. Satler, K.M. Kent, A.D. Pichard, N.J. Weissman, R. Waksman, Intravascular ultrasound parameters associated with stent thrombosis after drug-eluting stent deployment, Am. J. Cardiol. 100 (2007) 615–620.
[21] S.J. Kang, Y.R. Cho, G.M. Park, J.M. Ahn, W.J. Kim, J.Y. Lee, D.W. Park, S.W. Lee, Y.H. Kim, C.W. Lee, G.S. Mintz, S.W. Park, S.J. Park, Intravascular ultrasound predictors for edge restenosis after newer generation drug-eluting stent implantation, Am. J. Cardiol. 111 (2013) 1408–1414.
[22] S.Y. Choi, B. itzenbichler, A. Maehara, A.J. Lansky, G. Guagliumi, B. Brodie, M.A. Kellett Jr., O. Dressler, H. Parise, R. Mehran, G.D. Dangas, G.S. Mintz, G.W. Stone, Intravascular ultrasound findings of early stent thrombosis after primary percutaneous intervention in acute myocardial infarction: a Harmonizing Outcomes with Revascularization and Stents in Acute Myocardial Infarction (HORIZONS-AMI) substudy, Circ Cardiovasc Interv 4 (2011) 239–247.
[23] J. Pu, G.S. Mintz, S. Biro, J.B. Lee, S.T. Sum, S.P. Madden, A.P. Burke, P. Zhang, B. He, J.A. Goldstein, G.W. Stone, J.E. Muller, R. Virmani, A. Maehara, Insights into echo-attenuated plaques, echolucent plaques, and plaques with spotty calcification: novel findings from comparisons among intravascular ultrasound, near-infrared spectroscopy, and pathological histology in 2,294 human coronary artery segments, J. Am. Coll. Cardiol. 63 (2014) 2220–2233.
[24] S.J. Kang, J.M. Ahn, S. Han, D.W. Park, S.W. Lee, Y.H. Kim, C.W. Lee, S.W. Park, G.S. Mintz, S.J. Park, Multimodality imaging of attenuated plaque using grayscale and virtual histology intravascular ultrasound and optical coherent tomography, SJ. Catheter Cardiovasc. Interv. 88 (2016) E1–E11.
[25] S. Inaba, G.S. Mintz, A.P. Burke, G.W. Stone, R. Virmani, M. Matsumura,

R. Parvataneni, R. Puri, S.J. Nicholls, A. Maehara, Intravascular ultrasound and near-infrared spectroscopic characterization of thin-cap fibroatheroma, Am. J. Cardiol. 119 (2017) 372–378.
[26] M.I. Papafaklis, S. Takahashi, A.P. Antoniadis, A.U. Coskun, M. Tsuda, S. Mizuno, I. Andreou, S. Nakamura, Y. Makita, A. Hirohata, S. Saito, C.L. Feldman, P.H. Stone, Effect of the local hemodynamic environment on the de novo development and progression of eccentric coronary atherosclerosis in humans: insights from PREDICTION, Atherosclerosis 240 (2015) 205–211.
[27] R.D. Simmons, S. Kumar, H. Jo, The role of endothelial mechanosensitive genes in atherosclerosis and omics approaches, Arch. Biochem. Biophys. 591 (2016) 111–131.
[28] W. Fan, R. Fang, X. Wu, J. Liu, M. Feng, G. Dai, G. Chen, G. Wu, Shear-sensitive microRNA-34a modulates flow-dependent regulation of endothelial inflammation, J. Cell Sci. 128 (2015) 70–80.
[29] A. Materka, M. Strzelecki, Texture Analysis Methods–A Review, Technical university of lodz, institute of electronics, COST B11 report, Brussels, 1998, pp. 9–11.
[30] N. Zayed, H. Elnemr, Statistical analysis of Haralick texture features to discriminate lung abnormalities, J. Biomed. Imag. (2015) 267807.